PASJ: Publ. Astron. Soc. Japan **54**, 807–816, 2002 October 25

Spectroscopic Studies of the Solar Corona
III. Density Diagnostics Using the Infrared Lines of Fe XIII

Jagdev SINGH
Indian Institute of Astrophysics, Bangalore 560034, India
jsingh@iiap.ernet.in
Takashi SAKURAI and Kiyoshi ICHIMOTO
National Astronomical Observatory, 2-21-1 Osawa, Mitaka, Tokyo 181-8588
and
Aki TAKEDA*
Kwasan and Hida Observatories, Kyoto University, Sakyo-ku, Kyoto 606-8502

(Received 2002 April 8; accepted 2002 June 12)

Abstract

We have obtained spectrographic observations of several coronal regions in three emission lines (6374 Å [Fe X], 10747 Å [Fe XIII], and 10798 Å [Fe XIII]) simultaneously. The 25-cm coronagraph at Norikura Observatory and two large-format CCD cameras were used. The peak intensity, velocity, and line-width values were derived from Gaussian fits to the observed line profile at each location of the observed region. The ratio of the intensities of the 10747 Å and 10798 Å emission lines in the individual coronal structures range between 1.0 and 2.5 at $10''$ above the limb, which corresponds to a density range of 9.8×10^9–$2.4 \times 10^8\,\mathrm{cm}^{-3}$. The scale-height temperature values, derived from the variations of the intensity ratio with height above the limb for all individual coronal structures, range between 0.6×10^6 K and 8.3×10^6 K with a most frequent value around 1.8×10^6 K. The large values of the scale-height temperature for 70% of the structures indicate that these structures may not be in hydrostatic equilibrium nor be isothermal in nature.

Key words: line: profiles — Sun: corona — Sun: magnetic fields — techniques: spectroscopic

1. Introduction

Detailed knowledge of the electron density and its variation with time can yield important information about the physical and dynamical characteristics of the solar corona. The computation of scale heights from the measured values of densities along coronal structures will help to estimate their temperature and to make realistic models of the corona. The white-light pictures of the corona show the best the distribution of densities, because the amount of observed light is linearly related to the amount of free electrons and, consequently, to the plasma densities, integrated along the line-of-sight. The white-light pictures of the corona and measurements of the polarized continuum intensity during total solar eclipses have been used in determining the electron density in various kinds of coronal structures. Van de Hulst (1953) made the most comprehensive approach to the determination of the electron density by treating separately the intensities of the continuum (the so-called 'K-corona') that are polarized radially and tangentially to the surface. Newkirk (1961) determined the coronal densities based on non-eclipse measurements with the K-coronameter. Saito (1970) computed the radial variation in the electron density and constructed a non-spherical axisymmetric model for the corona at the minimum phase of the solar cycle. Not only plasma densities, but also temperature structures, can be easily and accurately analysed with ground-based coronagraphs (Altrock 1988). Koutchmy et al. (1991), using an instrument with good absolute calibration, deduced the radial variation of the electron densities in coronal loops, fine rays, enhancements, streamers, equatorial and polar regions, and coronal holes from an analysis of eclipse data. They assumed distributions of inhomogeneity in various degrees, and found large differences in the densities in coronal holes and loops. Orrall et al. (1990) studied the coronal density irregularities in the low corona based on measurements of the polarized brightness of the K-corona (pB), and the intensity of the strong resonance line of Mg X (625 Å) as a function of height between 1.05 and 1.25 solar radii. They found that the measured intensity of the [Mg X] line in the inner corona is much greater than that expected from the measured brightness, pB, based on the assumption that $n_{\mathrm{rms}} = n$. They interpreted this as being due to a coronal density irregularity much greater than unity, and suggested the existence of density fluctuations on small spatial scales associated with coronal heating. Guhathakurta et al. (1992) investigated the temperature and density within large-scale structures of the inner corona based on co-spatial and co-temporal data consisting of the following: coronal soft X-ray images near 173 Å observed from a sounding rocket; eclipse observations of the brightness in white light and in the coronal green line (5303 Å); and ground-based coronagraphic observations of the green and red (6374 Å) coronal lines. They found that the average of the ratio between the scale-height temperature and the temperature derived from the intensity ratio of the green and red lines over the entire range of position

---

[*] Presently at the Institute of Space and Astronautical Science, 3-1-1 Yoshinodai, Sagamihara, Kanagawa 229-8510, and at Solar Physics Research Corporation, 4720 Calle Desecada, Tucson, AZ 85718, U.S.A.

angles is roughly unity and between 1.3 and 1.6 in the prominent streamers.

All of these measurements give average values of the density in the corona. A more reliable technique for measuring the electron density in different parts of coronal structures and its variation with time would be to utilize the intensity ratios of proper line pairs which originate from the upper levels of the same ions with different density-dependent populations. This method has been extensively used to determine the electron density in the corona, flares, and active and quiet regions of the transition zone by means of soft X-rays and extreme ultraviolet lines (Landi, Landini 1997). Detailed reviews on this method and the most important results are found in Doschek (1990), Mason (1991), and Dwivedi (1993).

The observations of relative intensities of infrared coronal lines at 10747 Å and 10798 Å emitted by [Fe XIII] ions have been recognised as powerful tools for estimating the electron density in the emitting region. Finn and Landman (1973) made model calculations to derive the electron densities from the observed intensity ratios by taking into account additional factors, such as (i) collisional ionization and continuum radiative recombination processes, (ii) absorption of photospheric radiation with wavelength-dependent limb-darkening characteristics, and (iii) accurate proton rate constants. With the availability of large-format CCD cameras, it has now become possible to obtain the profiles of infrared lines emitted by [Fe XIII] ions in the corona with high spectral and spatial resolution. The temporal resolution still remains poor because of the long exposure times required due to the low efficiency of a CCD camera at these wavelengths, however. We have studied the intensity ratios of 10747 Å and 10798 Å emission lines from spectroscopic data obtained with the coronagraph at Norikura Observatory. In this paper we discuss the variations of the electron density in coronal structures and their changes with time. We also determined the scale height from the observed intensity variation as a function of height above the limb, and then computed the scale-height temperatures for different coronal structures assuming hydrostatic equilibrium and an isothermal nature of the coronal structures. An analysis of the line widths of the infrared lines will be published along with those of the red and green lines in a separate paper.

2. Observations

Spectroscopic observations in three coronal emission lines at 6374 Å (Fe X), 10747 Å (Fe XIII), and 10798 Å (Fe XIII) were made simultaneously with the 25-cm aperture coronagraph of the Norikura Solar Observatory in 1998 September and 1999 September, using two Peltier-cooled Photometrics CCD cameras. The first three columns of table 1 list the date, epoch, and observed coronal region. The coude-type coronagraph and a large Littrow-type spectrograph of 7 m focal length permitted us to observe two well-separated portions of the spectrum by using two CCD cameras (Singh et al. 1999). One CCD camera (made by Photometrics, Tucson, USA) of 512×512 format with a pixel size of $13.5\,\mu\text{m} \times 13.5\,\mu\text{m}$ was directly mounted at the focal plane of the Littrow focus of the spectrograph. This camera was used to obtain spectra around the red coronal emission line (third order). The second CCD camera of 1024×1024 format with a pixel size of $24\,\mu\text{m} \times 24\,\mu\text{m}$ coupled with a 20 cm aperture Cassegrain telescope was kept in the beam diffracted from the grating that spilled over the Littrow mirror. The Cassegrain telescope which focussed the spectrum on the second CCD camera was so arranged that we could obtain about a 60 Å portion of the spectrum in the second order, covering both the 10747 Å and 10798 Å [Fe XIII] lines. While recording the spectra, the CCD for the red line was binned both in spatial and wavelength directions by 2×2 pixels, and the CCD for the infrared lines was binned by 2 pixels in only the wavelength direction. The binned CCD output yielded a dispersion of 58 mÅ per pixel for the red line and 121 mÅ pixel^{-1} for the infrared lines. The large slit width of $160\,\mu$m used in the observations corresponded to 128 mÅ in the red-line spectra and 291 mÅ in the infrared-line spectra, respectively.

The glass block installed in front of the entrance slit was rotated stepwise to perform raster scans and to develop two-dimensional maps (spectroheliograms). Raster scans at 50 positions with a step of $4''$ were carried out with exposure times of 20–40 s for the red-line spectrum and 40–70 s for the infrared spectrum. To maintain simultaneity in the observations of both lines, the exposures for both of the CCD cameras were started at the same time and the CCD camera for the red-line spectrum waited to begin the next exposure until the exposure for the infrared spectrum was completed. One raster scan was completed in 30–60 min, depending on the exposure time for the infrared spectra which was always greater than that for the red line. On each day, two or three regions were chosen for observations, and raster scans were repeated on these regions in a cyclic order while the sky permitted.

3. Data Analysis

The pixel resolution of the spectroheliograms after binning the CCD readout was about $2'' \times 2''$, but the slit width that was equivalent to $4''$ on the Sun restricted the spatial resolution to $2'' \times 4''$. All of the spectra were corrected for the dark current and the flat field, and the sky component obtained from a spectrum of defocussed solar disc image was subtracted. In the top panel of figure 1a we show a typical observed profile of the red coronal emission line. The bottom panel shows the residual emission profile after the dark current and flat field corrections, and then subtracting the scattered-light component due to sky brightness. A Gaussian fit to the residual profile is also plotted. Figure 1b shows a typical observed profile of the infrared coronal emission lines, the corrected profiles, and the Gaussian fits. The fitting errors in the estimated parameters of the line profiles are listed in table 2 for points near the limb and at $100''$ above the limb. The fitting was made by discarding the data points at the locations of the absorption lines near the emission lines, to make sure of the reliability of the fit. Table 2 indicates very small errors in the computed values of the relative amplitude, central wavelength, and FWHM from the Gaussian fits to the data. Almost in all cases a single Gaussian fit to the observed emission-line profile was found to be satisfactory; at no instance did the observed line profiles show double peaks. Plots of these values of line parameters give us spectroheliograms, Dopplergrams, and line-width maps. Figure 2 is a typical example of such an analysis. The top left and right panels

Table 1. Average values of electron density at 10″ above the limb, and scale height and scale-height temperature over all the coronal structures in the observed region.

Date yy/mm/dd	Epoch UT	Coronal region	Intensity ratio[†] at 10″	log of n_e (cm^{-3}) at 10″	Intensity ratio[†] at $1/e$ density	Scale height (arcsec)	Scale-height temperature ($\times 10^6$ K)
98/09/09	2204	South-west	2.22	8.509	3.27	422	6.1
	2334		2.10	8.574	3.07	388	5.6
	2227	North-west	2.20	8.520	3.24	183	2.6
	2306		2.08	8.591	3.03	232	3.3
98/09/10	0014		2.14	8.558	3.13	229	3.3
98/09/12	0423	North-west	1.41	9.148	1.88	307	4.4
	0536		1.35	9.247	1.75	223	3.2
	0644	South-west	2.03	8.616	2.97	87	1.2
98/09/12	2135	South-west	1.37	9.214	1.79	65	1.0
	2252		1.63	8.919	2.27	107	1.5
98/09/13	0155		2.12	8.563	3.10	454	6.5
	0704		1.88	8.719	2.72	506	7.3
	0751		1.75	8.818	2.48	412	5.9
98/09/12	2358	North-east	1.97	8.684	2.80	105	1.5
98/09/13	0603	East	1.52	9.024	2.08	70	1.0
	0059	North-west	2.05	8.601	3.01	154	2.2
98/09/13	2125	South-west	1.78	8.783	2.56	414	5.9
	2349	North-east	1.64	8.910	2.29	154	2.2
98/09/14	0026		1.45	9.118	1.94	103	1.5
	0244		1.51	9.028	2.08	166	2.4
99/09/27	2304	South-east	1.66	8.907	2.34	123	1.8
99/09/28	0046		1.51	9.033	2.07	99	1.4
99/09/28	0243	East	1.49	9.054	2.02	118	1.7
	0155		1.47	9.088	1.98	64	0.9
	0208		1.46	9.087	1.98	65	0.9
99/09/27	2348	North-west	1.74	8.849	2.42	415	6.0
99/09/28	0305		1.75	8.814	2.49	434	6.2
99/09/28	2232	South-east	1.34	9.266	1.73	51	0.7
	2254		1.59	8.963	2.19	177	2.5
	0057	North-west	1.72	8.837	2.44	147	2.1

[†] $I(10747)/I(10798)$.

show the intensity distribution, the middle two panels show the velocity distribution, and the bottom two panels indicate the line-width distribution in the 10747 Å and 10798 Å lines, respectively, for a coronal region observed on 1998 September 9. The top panels of this figure indicate a one-to-one resemblance between the 10747 Å and 10798 Å line features, as expected. The line widths appear to indicate a small change with height along the coronal structure, which will be investigated later in combination with the red-line data. Figure 3 shows some of the coronal regions observed on different days.

To study the ratio of the 10747 Å and 10798 Å line intensities in different coronal structures and its variation with time, we performed analyses of the data in two ways. In one method we considered all of the fine structures together in the observed coronal region to derive the intensity ratios of these two lines. We displayed the spectroheliograms of the 10747 Å and 10798 Å lines on the computer screen and then selected a point on a coronal structure seen in the image of the 10747 Å line with the help of the cursor. The corresponding location in the image of the 10798 Å line was automatically identified by the developed computer program. The intensity values at this point and the position of the selected point were stored in a file. The spatial resolution of the point was 4″ × 4″. In this way we selected 100–200 points along all the structures in the observed coronal region consisting of about 115 × 40 pixels, and used the data to investigate the average physical characteristics of the region. In figure 4, the small white squares added to figure 2 show the locations on the coronal structures over which the intensity values were determined for the data of 1998 September 9.

The second method we adopted was to mark 10–20 small boxes along only one of the fine structures in the observed region, and thus investigate the behavior of the individual structures. The spectroheliograms in figures 2 and 3 indicate that these structures have widths of 4″–20″. Therefore, to study the average behavior of the variations and the relation between

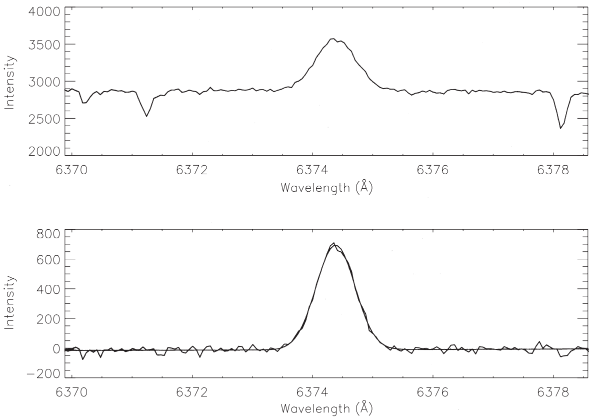

Fig. 1a. The upper panel shows a typical observed profile for the red line at 6374 Å. The lower panel shows the residual profile after corrections for the dark current, flat field, and scattered light due to sky brightness. A Gaussian fit to the residual data is also shown.

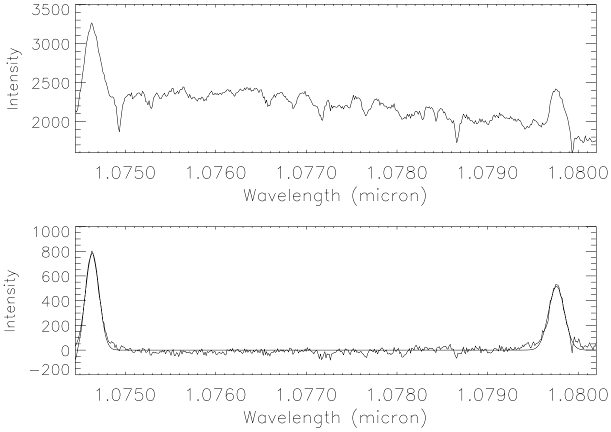

Fig. 1b. The upper panel shows a typical observed profile for the infrared 10747 Å and 10798 Å emission lines. The lower panel shows the residual profile after corrections for the dark current, flat field, and scattered light due to sky brightness. A Gaussian fit to the residual profile is also shown.

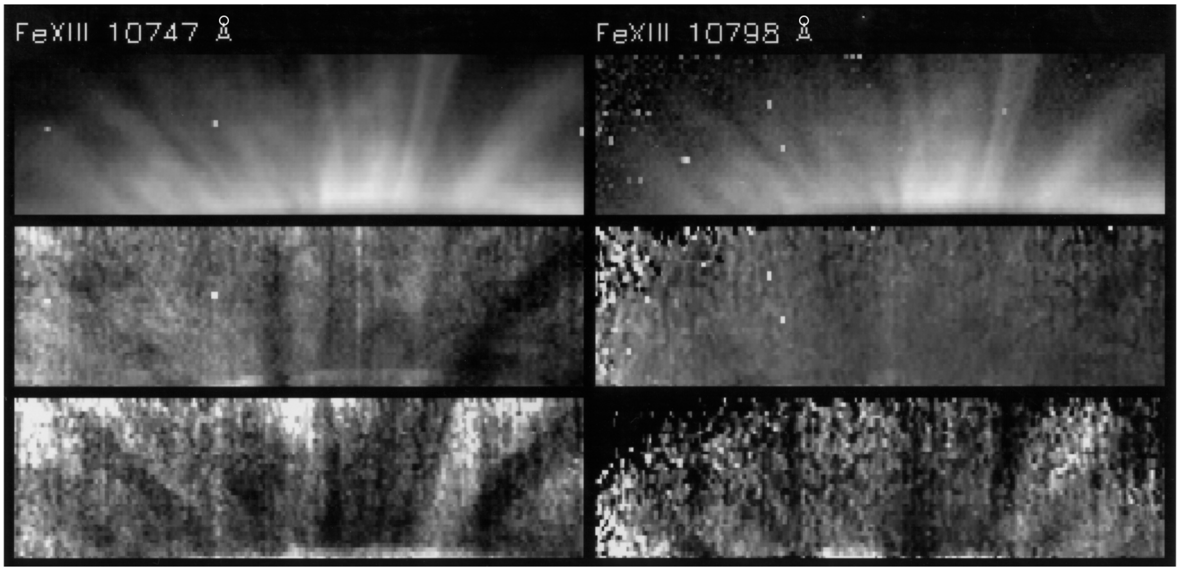

Fig. 2. Images of the solar corona constructed from the line profiles observed on 1998 September 9. The top row shows the distribution of 10747 Å and 10798 Å line intensities in the observed coronal region. The middle and bottom rows indicate the velocity and line-width distributions, respectively.

these two intensities, we marked small boxes instead of points in the 10747 Å line image, as can be seen in figure 5. The corresponding box was automatically identified in the image of the 10798 Å line with the help of the computer program, and the average values of the intensities of the 10747 Å and 10798 Å lines in the selected box were computed. The size of the box varied randomly between $8'' \times 8''$ and $12'' \times 20''$ according to the shape and size of the structure. Most of the time these boxes were rectangular in nature, and sometimes square.

Once the intensity ratio, $I(10747)/I(10798)$, was obtained, we could convert it to the electron density. The calculation of Finn and Landman (1973) assumed a dilution factor for the photospheric radiation field of 0.5. The structures we studied were distributed in height range up to $250''$, which corresponds to a dilution factor of 0.2. Flower and Pineau des

Table 2. Typical errors in the computed relative intensity, FWHM, and central wavelength from the Gaussian fit.

	10747 Å line	10798 Å line
Near the limb:		
Relative intensity	±0.050%	±0.075%
FWHM	±0.001 Å	±0.002 Å
Wavelength	±0.001 Å	±0.001 Å
At $100''$ above the limb:		
Relative intensity	±1.2%	±0.26%
FWHM	±0.002 Å	±0.004 Å
Wavelength	±0.002 Å	±0.002 Å

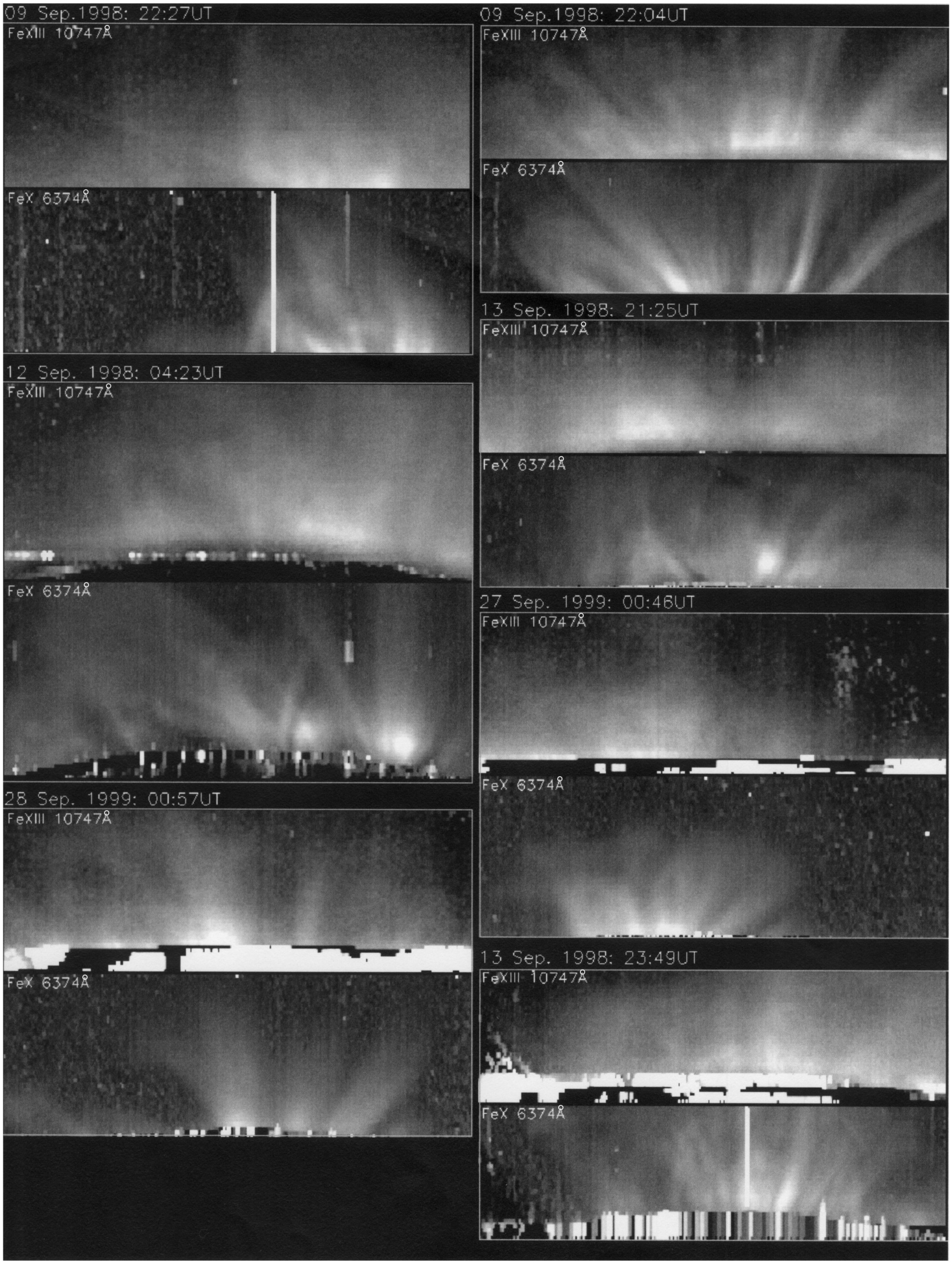

Fig. 3. Spectroheliograms of the 6374 Å and 10747 Å coronal emission lines of several regions observed on different days. A date is given above each image.

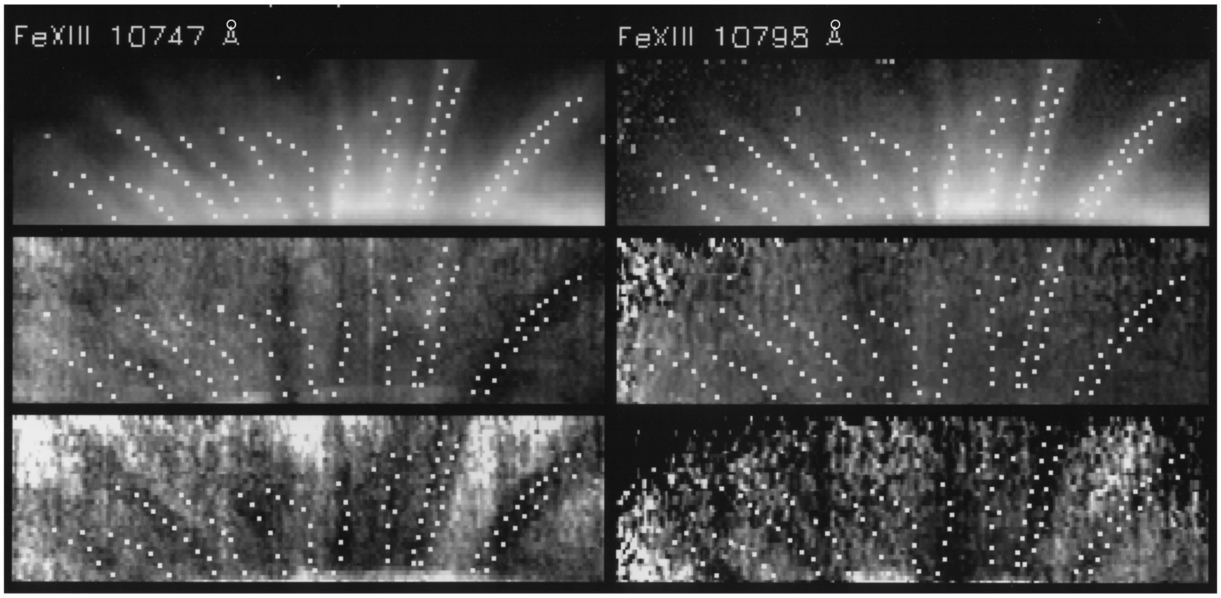

Fig. 4. Same as figure 2. In addition, small white squares show the locations on the coronal structures over which the intensity values were determined to study the average characteristics of the region.

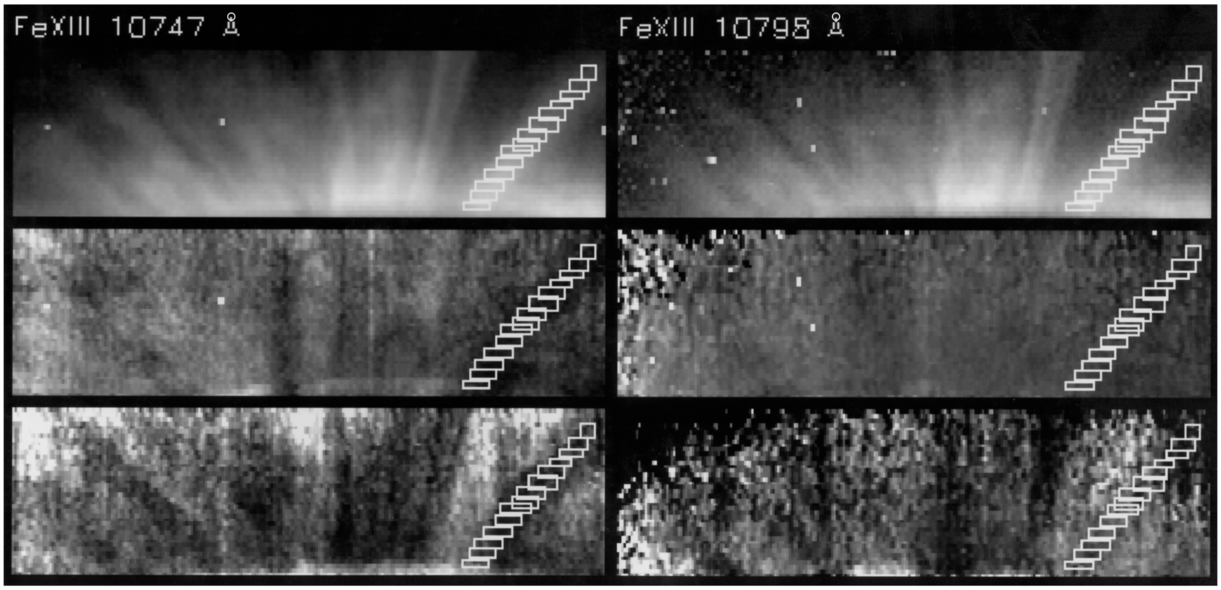

Fig. 5. Same as figure 2. In addition, it shows small white boxes marked on a coronal structure. The average values of the intensity, velocity, and line width in each small coronal region marked by the box have been computed. The box size varied depending on the size and shape of the coronal structure.

Forêts (1973) computed the intensity ratios for various dilution factors. However, their figure 5 indicates that the values of the dilution factor ranging from 0.1 to 0.5 yield almost the same intensity ratio of $I(10747)/I(10798)$ for electron densities of 3×10^{8}–$10^{10}\,\mathrm{cm}^{-3}$, which entirely cover the density range that we observed. Therefore, the use of Finn and Landman's (1973) results may be justified. Figure 6 shows the conversion curve that we used, taken from figure 1 of Finn and Landman (1973).

Recent spectroscopic diagnostic packages, such as CHIANTI (Dere et al. 2001), are based on a more recent atomic database. A comparison between CHIANTI and Finn and Landman (1973) for Fe XIII shows that the two results are not very different (P. R. Young, private communication).

4. Results

We obtained the spectra in the red and infrared lines on six days between 1998 September 10 and 14 and 1999 September 27–28.

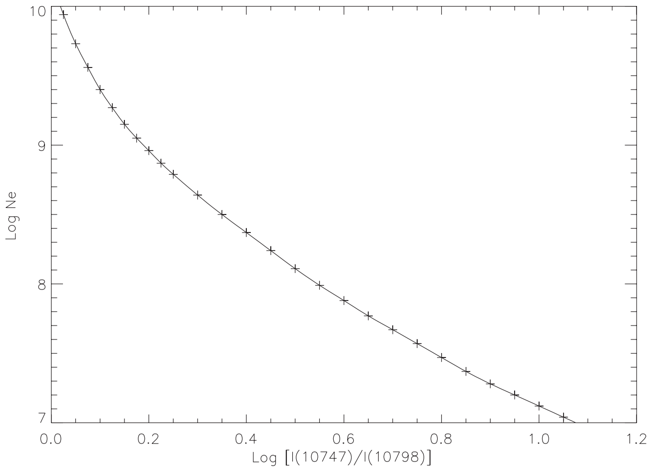

Fig. 6. Plot of the electron density versus the ratio between the 10747 Å and 10798 Å line intensities [adapted from Finn and Landman (1973)].

4.1. *Intensity Ratio of Infrared Lines: All Structure Included*

Figure 7 is a typical example obtained by considering all of the structures together in an observed region. The upper panel shows a plot of the 10747 Å line intensity [hereafter referred as $I(10747)$] versus 10798 Å line intensity [$I(10798)$] along with a linear fit to the data. The lower panel of the figure shows the ratio $I(10747)/I(10798)$ as a function of height above the solar limb. Both figures show scatter, possibly because different individual structures have different physical characteristics. The ratio plot shows almost a linear variation between the intensity ratio and height. The values of $I(10747)/I(10798)$ at $10''$ above the limb and at the height where the density drops by $1/e$ from the limb were computed by using a linear fit to the data. A conversion between the intensity ratio and the density was made using the curve shown in figure 6. Table 1 lists the intensity ratio at $10''$ and at $1/e$ density and log(density) at $10''$. The average density in coronal structures varied between $2.8 \times 10^8\,\mathrm{cm}^{-3}$ and $3.2 \times 10^9\,\mathrm{cm}^{-3}$ at $10''$ above the limb. Table 1 also gives the average values of the scale height in arcsecond and the scale-height temperature for several coronal regions observed.

4.2. *Temporal Variations in Coronal Structures*

We could only observe most of the coronal regions for a short duration of 1–2 hours because of unstable sky conditions. Only on 1998 September 13 could we observe a coronal region for about 10 hours. Table 1 indicates that on 1998 September 12 at 21:35 UT the mean electron density at $10''$ above the limb was about $1.6 \times 10^9\,\mathrm{cm}^{-3}$ and the scale-height temperature was about $1.0 \times 10^6\,\mathrm{K}$. During an interval of 10 hours the electron density decreased to $6.5 \times 10^8\,\mathrm{cm}^{-3}$ at a height of $10''$ and the scale-height temperature increased to $5.9 \times 10^6\,\mathrm{K}$. It is difficult to say how the changes in these parameters occurred because of a large gap of about five hours in the observations.

4.3. *Intensity Ratio of Infrared Lines: Individual Structures*

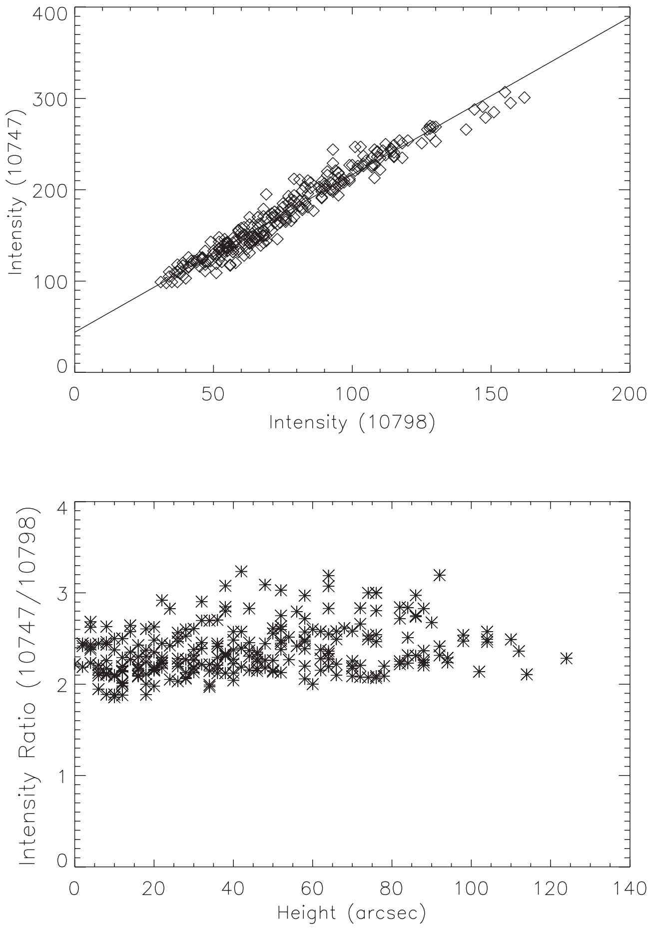

Fig. 7. Plots of the intensity and intensity ratio of the 10747 Å and 10798 Å lines, obtained by selecting small squares on all of the structures in the coronal region. The size of the selected square was $4'' \times 4''$.

Figure 8 is a typical example obtained by selecting 12 small coronal regions on an individual structure. The top panel shows a plot of $I(10747)$ versus $I(10798)$, the middle panel shows the FWHM of 10747 Å and 10798 Å emission lines as a function of height, and the bottom panel shows the ratio $I(10747)/I(10798)$ as a function of height above the limb along with a linear fit to the data. The figure indicates much less scatter in the data as compared to that while considering all of the structures together. This confirms that different individual structures in a coronal region have different physical conditions. The intensity ratios $I(10747)/I(10798)$ at $10''$ above the limb and at $1/e$ density were computed from the linear fit to the data of individual structures. Figure 9 shows the frequency distribution of log(density) at $10''$ above the limb. The density in the coronal structures at $10''$ range between $2.4 \times 10^8\,\mathrm{cm}^{-3}$ to $9.8 \times 10^9\,\mathrm{cm}^{-3}$, and the distribution is broad with a mean value of $7.9 \times 10^8\,\mathrm{cm}^{-3}$.

4.4. *Intensity Ratio of Red to Infrared Lines: Individual Structures*

We have also analyzed the data of the 6374 Å and 10747 Å lines by selecting 10–20 small boxes along a coronal structure in a method similar to that adopted for the 10747 Å and 10798 Å data. The observed line intensity was corrected for the exposure time and the wavelength response of the CCD camera by using spectra at the center of the defocussed solar

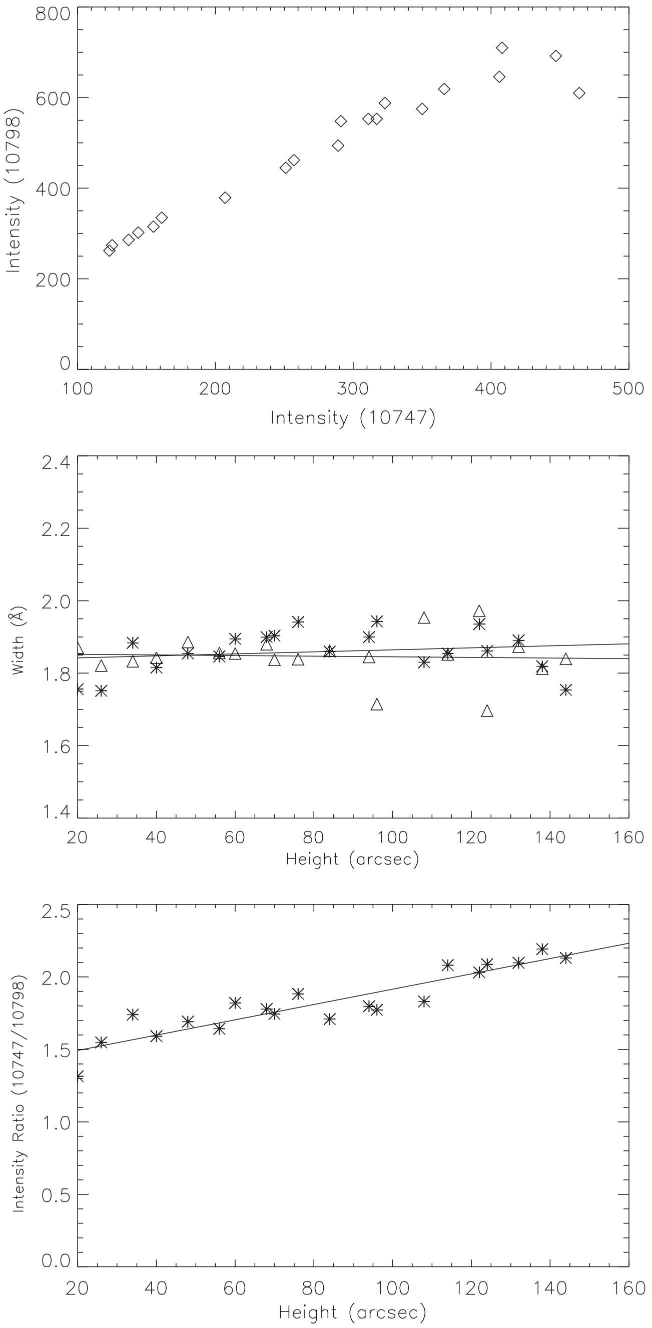

Fig. 8. Plots of the intensity and intensity ratio of 10747 Å and 10798 Å lines obtained by marking boxes on an individual coronal structure. The top panel shows the 10798 Å line intensity versus the 10747 Å line intensity. The middle panel shows the FWHM of the two lines as a function of height. The bottom panel shows the intensity ratio $I(10747)/I(10798)$ as a function of height along with a linear fit to the observed data.

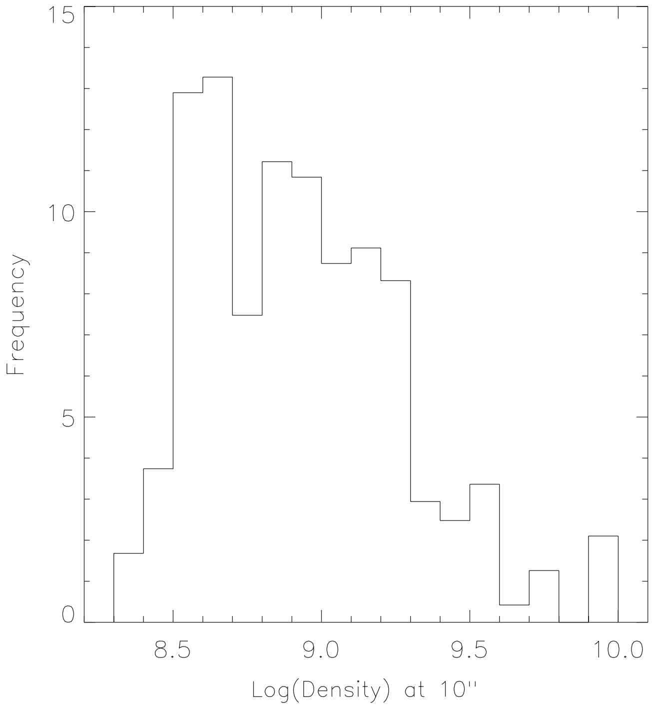

Fig. 9. Frequency distribution of log(density) at 10$''$ above the limb.

disc. The top panel of figure 10 shows a plot of 6374 Å line intensity versus 10747 Å line intensity along with a linear fit to the data. The middle panel shows the FWHM of the two lines as a function of height above the limb. The bottom panel shows the intensity ratio between 6374 Å and 10747 Å lines as a function of height. The intensity ratio ranges between 1.8 and 7.4 for the observed individual coronal structures and the ratio decreases with height above the limb for almost all of the structures. The decrease in the ratio may imply an increase in temperature along the coronal structure toward its top.

4.5. *Scale-Height Temperatures*

We have determined the variation in the ratio $I(10747)/I(10798)$ as a function of height above the solar limb in all the individual coronal structures which we found to vary linearly with height. Our data extends to only about 250$''$ above the limb. Therefore, we made a linear fit to the observed intensity ratios as a function of height in the individual coronal structure to derive the value of the scale-height parameter for that structure. The variations in the electron density were computed using the relationship between the intensity ratio and the electron density, as shown in figure 6. We then derived the scale height for each coronal structure, i.e., the height at which the electron density falls to $1/e$ of the density at the base of the coronal structure. We could determine the scale height of 250 individual structures in 15 different coronal regions observed between 1998 September 10 and 14 and 1999 September 27–28. In table 1 we list the mean values of the scale height and the corresponding values of the scale-height temperature for several regions. We also find that there are large variations in the values of the scale height among individual structures in a coronal region. The scale height varied by a factor of 3 in some coronal regions.

Considering all of the coronal structures together, we plotted the frequency distribution of the scale-height values in figure 11. The figure shows that the scale height ranges between 34$''$ and 742$''$ for the observed coronal structures, with the most frequent value being around 125$''$. If we assume that the plasma in emission-line coronal structures is isothermal along the line-of-sight and in radial hydrostatic

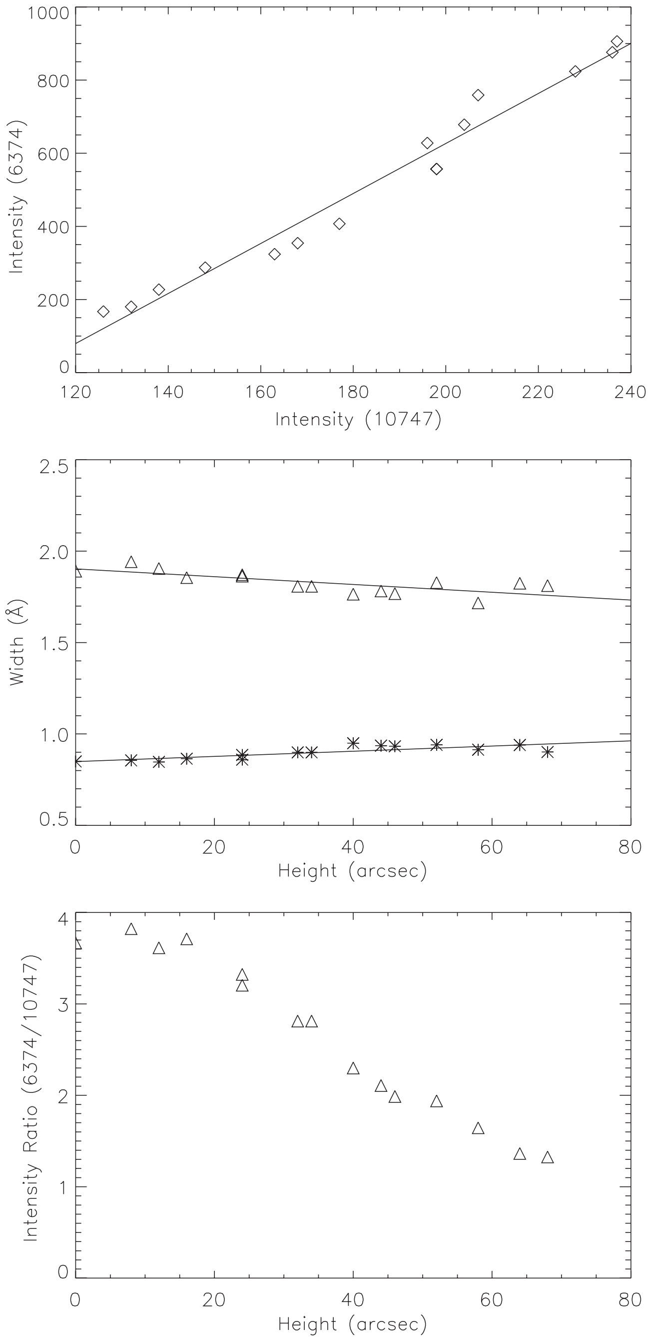

Fig. 10. The top panel shows 6374 Å line intensity versus 10747 Å line intensity along with a linear fit to the data for an individual structure. The variations of FWHM of the two lines and intensity ratio as a function of height above the limb are shown in the middle and bottom panels, respectively.

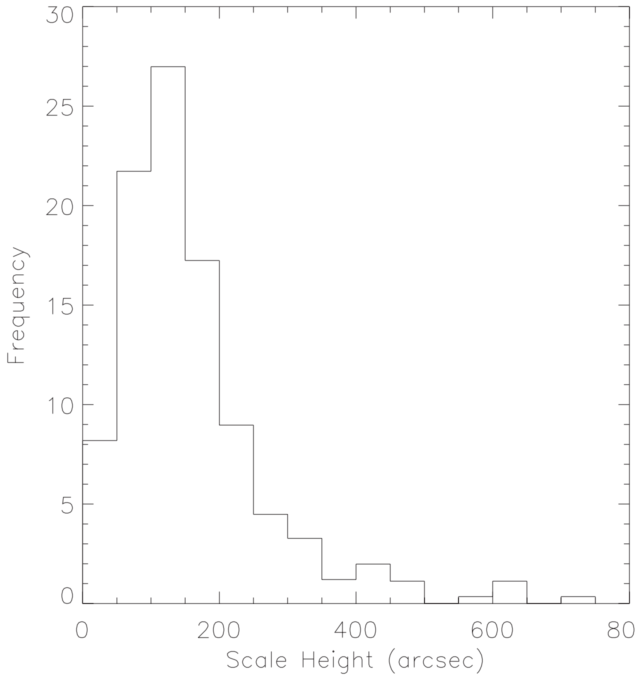

Fig. 11. Histogram of scale heights derived from the analysis of 250 individual structures.

equilibrium, the relation between the scale-height parameter and the scale-height temperature can be defined as (Orrall et al. 1990; Guhathakurta et al. 1992)

$$h_{\odot} = \frac{kT_{\rm s}}{mg_{\odot}R_{\odot}}, \tag{1}$$

where $h_{\odot}$ is the density scale-height parameter expressed in units of the solar radius, $R_{\odot} = 6.96 \times 10^{10}\,\rm cm$. Here, $g_{\odot} = 2.74 \times 10^{4}\,\rm cm\,s^{-2}$ is the Sun's surface gravity and m is the mean particle mass (in the inner corona it is about 0.625 times the proton mass). Substituting these values, the above relation can be written (Guhathakurta et al. 1992) as

$$h_{\odot} = 0.0729 \times 10^{-6} T_{\rm s}, \tag{2}$$

where $T_{\rm s}$ is the scale-height temperature (that is, the temperature implied by the scale height assuming hydrostatic equilibrium). The most frequent value of the observed scale height (125″) implies a scale-height temperature of $1.8 \times 10^{6}\,\rm K$. However, about 55% of the coronal structures indicate a scale height larger than 125″, and about 20% of the observed structures show values greater than 200″. The scale heights of 100″ and 200″ imply scale-height temperatures of $1.5 \times 10^{6}\,\rm K$ and $2.9 \times 10^{6}\,\rm K$, respectively.

Figure 12 shows the electron density at 10″ above the limb against the derived scale height. This plot indicates that denser loops have smaller scale heights. The relationship between these two parameters can be conveniently described by a modified exponential function,

$$\log n_{\rm e}({\rm cm}^{-3}) = ae^{b/h}, \tag{3}$$

where h is the scale height in arcsecond, $a = 8.68$, and $b = 2.''86$. The correlation coefficient is 0.69 with a confidence level of 99%.

5. Discussions

All of the structures under investigation were, of course, associated with active regions, but were steady and quiet during the period of observations. We detected no flares or prominence eruptions in this region. The minimum value of 1.0 of the observed intensity ratio in coronal structures corresponds to

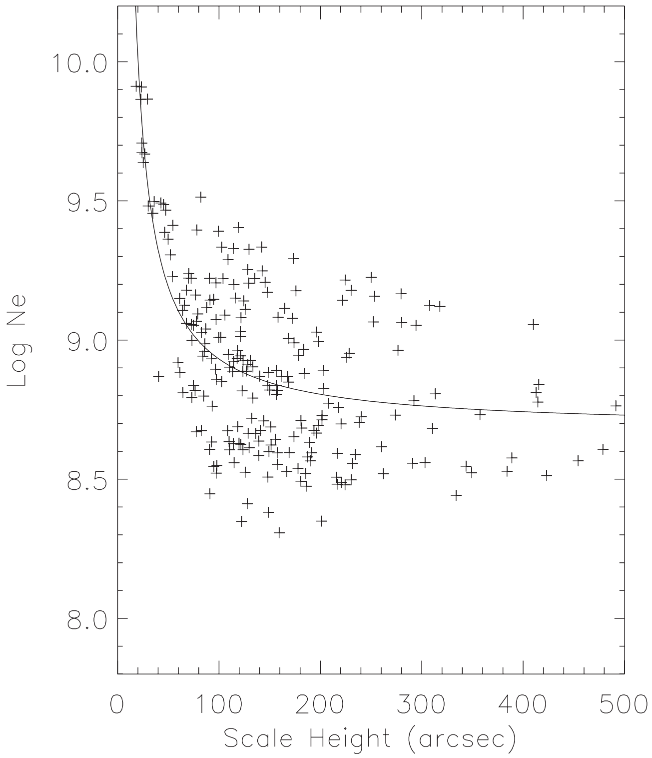

Fig. 12. Plot of log(density) at 10″ above the limb against scale height in arcsecond.

an electron density of $9.8 \times 10^9\,\mathrm{cm}^{-3}$, and the observed maximum value of 3.1 corresponds to $1.4 \times 10^8\,\mathrm{cm}^{-3}$. In all of the individual coronal structures, the value of the intensity ratio increased with height above the solar limb, which implies that the electron density decreases with height, as expected. About 70% of the coronal structures show a scale height larger than 100″. This suggests that these structures are at a temperature of more than 1.5×10^6 K, assuming the hydrostatic equilibrium and an isothermal nature of the coronal structures. The ratio of the 6374 Å line intensity to the 10747 Å line intensity for an individual structure ranges between 0.6 and 7.4, which implies an average temperature of about 1.5×10^6 K for these coronal structures. The values of the scale-height temperature are higher than this for 70% of the structures. Therefore, we may conclude that these structures are neither isothermal nor in hydrostatic equilibrium. A non-uniformity in temperature along the coronal structure is also indicated by the variation in the ratio of 6374 Å to 10747 Å line intensity as a function of height above the limb. A more important conclusion here, however, is a prevailing tendency of the violation of hydrostatic equilibrium. This may point toward dynamic, non-steady loop models proposed e.g. by Kuin and Martens (1982).

Part of this work was carried out while JS was a visiting scientist at the National Astronomical Observatory of Japan. He thanks the staff of the Solar Physics Division and the Norikura Solar Observatory for their hospitality which made his stay comfortable at Norikura and Mitaka.

References

Altrock, R. C. 1988, in Solar and Stellar Coronal Structure and Dynamics: Proc. of the 9-th Sacramento Peak Summer Symp., ed. R. C. Altrock (Sunspot, NM: National Solar Observatory), 414
Dere, K. P., Landi, E., Young, P. R., & Del Zanna, G. 2001, ApJS, 134, 331
Doschek, G. A. 1990, ApJS, 73, 117
Dwivedi, B. N. 1993, Space Sci. Rev., 65, 289
Finn, G. D., & Landman, D. A. 1973, Sol. Phys., 30, 381
Flower, D. R., & Pineau des Forêts, G. 1973, A&A, 24, 181
Guhathakurta, M., Rottman, G. J., Fisher, R. R., Orrall, F. Q., & Altrock, R. C. 1992, ApJ, 388, 633
Koutchmy, S., Zirker, J. B., Steinolfson, R. S., & Zhugzda, J. D. 1991, in Solar Interior and Atmosphere, ed. A. N. Cox, W. C. Livingston, & M. S. Matthews (Tucson, AZ: Univ. of Arizona Press), 1044
Kuin, N. P. M., & Martens, P. C. H. 1982, A&A, 108, L1
Landi, E., & Landini, M. 1997, A&A, 327, 1230
Mason, H. E. 1991, Adv. Space Res., 11, 293
Newkirk, G., Jr. 1961, ApJ, 133, 983
Orrall, F. Q., Rottman, G. J., Fisher, R. R., & Munro, R. H. 1990, ApJ, 349, 656
Saito, K. 1970, Annals Tokyo Astron. Obs., 2nd Ser., 12, 53
Singh, J., Ichimoto, K., Imai, H., Sakurai, T., & Takeda, A. 1999, PASJ, 51, 269
Van de Hulst, H. C. 1953, in The Sun, ed. G. P. Kuiper (Chicago, IL: Univ. of Chicago Press), 207